

Magneto-optical properties of Group-IV–vacancy centers in diamond upon hydrostatic pressure

Meysam Mohseni,^{1,2} Lukas Razinkovas,³ Vytautas Žalandauskas,³ Gergő Thiering,¹ and Adam Gali^{1,4,5}

¹*HUN-REN Wigner Research Centre for Physics, PO. Box 49, H-1525 Budapest, Hungary*

²*Loránd Eötvös University, Pázmány Péter Sétány 1/A, H-1117 Budapest, Hungary*

³*Center for Physical Sciences and Technology (FTMC), Vilnius LT-10257, Lithuania*

⁴*Budapest University of Technology and Economics,
Műegyetem rakpart 3., H-1111 Budapest, Hungary*

⁵*MTA-WFK Lendület "Momentum" Semiconductor Nanostructures Research Group, PO. Box 49, H-1525 Budapest, Hungary*

(Dated: August 21, 2024)

In recent years, the negatively charged group-IV–vacancy defects in diamond, labeled as G4V(–) or G4V centers, have received a great attention in quantum information processing. In this study, we investigate the magneto-optical properties of the G4V centers under high compressive hydrostatic pressures up to 180 GPa. The spin-orbit splitting for the electronic ground and excited states and the hyperfine tensors are calculated by means of plane wave supercell density functional theory as unique fingerprints of these defects. To this end, we developed a theory for calculating the hyperfine tensors when the electronic states are subject to Jahn–Teller effect. We find that the zero-phonon-line energy increases with adding hydrostatic pressures where the coupling strength increases from SiV(–) to PbV(–). On the other hand, the calculated photoionization threshold energies indicate that the operation of PbV(–) based quantum sensor is limited up to 30 GPa of hydrostatic pressure whereas SnV(–), GeV(–) and SiV(–) remain photostable up to 180 GPa of hydrostatic pressure.

I. INTRODUCTION

The negatively charged group-IV–vacancy (G4V) defects in diamond, i.e., G4V(–) defects or G4V centers, have gained substantial attention in the last decades (see the schematic geometry and electronic structure in Fig. 1). These color centers including silicon-vacancy (SiV), germanium-vacancy (GeV), tin-vacancy (SnV), and lead-vacancy (PbV) defects are promising qubits for quantum communication and sensor applications [1–23]. The G4V centers have $S = 1/2$ spin state and exhibit D_{3d} inversion symmetry [24–26] which leads to extraordinary optical stability when compared to other color centers such as nitrogen-vacancy center in diamond [27, 28], which can be utilized in quantum communication technologies [21, 22]. The electronic structure of G4V centers provides an advantage to achieve coherent control of spin states using only optical methods, without the need for microwave fields [29–34]. The ability of microwave-free control of spin states can be practical under extreme conditions such as high pressures where the reduction of the complexity of measurement is a very important issue [19]. On the other hand, the effect of pressure on the magneto-optical properties of the G4V centers has not yet been explored in details [19, 35] which is an inevitable step to determine the potential of these color centers in high-pressure quantum sensor applications.

In this paper, we explore the magneto-optical properties of G4V centers upon compressive hydrostatic pressure by means of density functional theory plane wave supercell calculations. In particular, we focus on the fine level structure of the electronic structure, i.e., the spin-orbit and hyperfine interaction in the respective ground state and excited state. These properties are intertwined with the strong electron-phonon coupling that can be de-

scribed by the Jahn–Teller theory [26]. We developed a theory to accurately compute the hyperfine tensors subject to the Jahn–Teller effect and implemented it to calculate all the critical hyperfine tensor elements of the respective group-IV dopant and the proximate ¹³C nuclear spins. The photoionization threshold energies are also monitored in our study, along with the shift in the zero-phonon-line energy as a function of compressive hydrostatic pressure. We provide the list of pressure-dependent magneto-optical parameters which indicate the coupling strength of pressure to zero-phonon-line (ZPL) energies, spin-orbit gaps, and hyperfine levels. These parameters can be used to calibrate the actual pressure acting on the color centers. We find that the coupling strength increases when going from lighter to heavier group-IV element in the G4V centers. Our calculations also reveal that the operation of the PbV(–) quantum sensor is limited up to 32 GPa.

II. METHODS

We employed density functional theory (DFT) calculations [36, 37] using plane-wave supercell and the projector-augmented-wave (PAW) approach [38, 39] as implemented in the Vienna Ab-initio Simulation Package (VASP) [40, 41]. The exchange-correlation functional of strongly constrained and appropriately normalized (SCAN) meta-GGA was employed [42]. For the hyperfine tensor calculations, we also list results with HSE06 functional [43]. The defect structure is simulated within a $4 \times 4 \times 4$ supercell, which consists of 512 atoms with a lattice constant of 14.21 Å and 14.18 Å in the SCAN and hybrid functional, respectively. Γ -point was used for sampling the Brillouin-zone. The structures op-

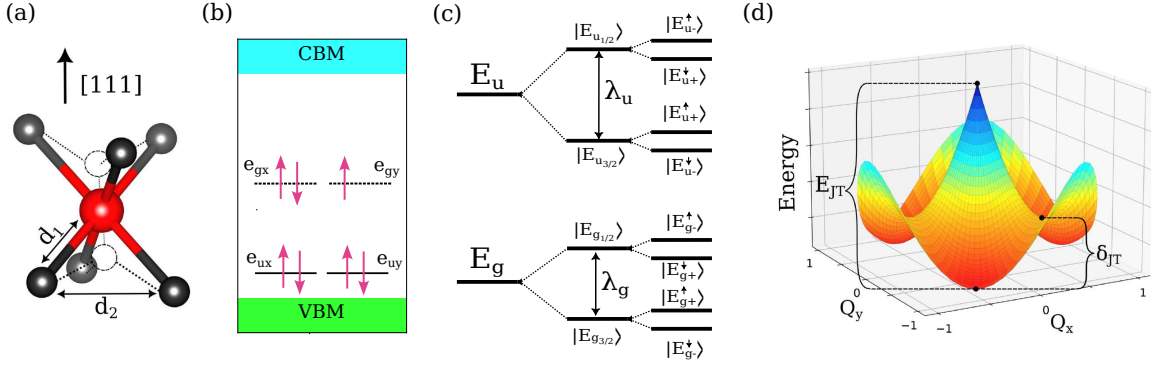


FIG. 1. Schematic diagrams about the basic properties of G4V(−) color centers in diamond. (a) Geometry of the defect. The two vacancies and the interstitial dopant atom (silicon, germanium, tin, or lead) are labeled by dashed spheres and a red sphere, respectively. The critical distances under high D_{3d} symmetry are labeled by d_1 and d_2 . The dopant atom sits in the inversion center of the diamond. (b) Defect levels in the electronic ground state. The positions of the fully occupied double degenerate e_u levels and the partially occupied e_g levels vary in the various G4V(−) color centers. In the electronic excited state (not shown) the e_g levels are fully occupied whereas a hole is left on the e_u level. (c) Electronic structure in the ground and excited states. $\lambda_{g,u}$ are the effective spin-orbit splitting in the g (even parity) ground and u (odd parity) excited states. The effect of the applied magnetic field (significantly smaller than $\lambda_{g,u}$) is also depicted. (d) Adiabatic potential energy surface (APES) of the quadratic Jahn–Teller system with single effective symmetry breaking phonon. $Q_{x,y}$ configuration coordinates represent the effect of the symmetry-breaking degenerate e_g phonon on the APES of which frequency is given by the steepness of the paraboloids. E_{JT} is the difference in energy between the high symmetry configuration and the distorted configuration. The three equivalent global minima are separated by energy barriers of δ_{JT} .

timized with the criterion of 10^{-2} eV/Å per atom for the Hellman-Feynman forces and a kinetic energy cutoff of 600 eV was used. The geometry optimization of the electronic excited state is carried out by the Δ SCF method [44] so the ZPL energies are computed as the total energy difference in the respective electronic states in their global adiabatic potential energy surface minima.

Next, we discuss the spin-orbit coupling and hyperfine tensor calculations which yield the fine electronic structure of G4V(−) defects. We determined the spin-orbit coupling (SOC) with SCAN functional in the non-collinear approach for the G4V centers by using the quantization axis of the spin along the symmetry axis of the defect. The SOC has a small perturbation effect on electronic states, therefore we calculate it in the optimized high D_{3d} symmetry configuration. G4V(−) defects have double degenerate $e_{g\{x,y\}}$ states in the gap that are occupied with three electrons, which can be considered as single hole occupation of the double degenerate $e_{g\{x,y\}}$ states. After applying the SOC on the system, the associated z component of SOC, λ_0 , splits the $e_{g\pm} = (\frac{1}{\sqrt{2}})(e_{gx} \pm ie_{gy})$ states. We applied Δ SCF method to either occupy e_{gx} or e_{gy} spinor state (constraint occupation of Kohn-Sham orbitals, e.g., Ref. 44). The Hamiltonian of SOC is given by

$$\hat{H}_{\text{SOC}} = -\lambda_0 \hat{L}_z \hat{S}_z = \frac{\lambda_0}{2} \left[|e_{g+}^\dagger\rangle \langle e_{g+}^\dagger| + |e_{g-}^\dagger\rangle \langle e_{g-}^\dagger| - |e_{g-}^\dagger\rangle \langle e_{g-}^\dagger| - |e_{g+}^\dagger\rangle \langle e_{g+}^\dagger| \right], \quad (1)$$

where the \hat{L}_z is the orbital moment operator and \hat{S}_z is the z component of the electronic spin. The negative sign of λ_0 occurs because of the hole quasiparticle.

The hyperfine (HF) interaction refers to the coupling between nuclear spins and the electron spin, causing additional splitting of spectral lines in the electron spin resonance spectrum. This provides a unique fingerprint of atomic structure when the spin density has an overlap with the nuclear spins. The hyperfine tensor is expressed as

$$A_{ij}^{(I)} = \frac{1}{2S} \int d^3r \rho_s(r) \gamma_I \gamma_e \hbar^2 \times \left[\left(\frac{8\pi}{3} \delta(r) \right) + \left(\frac{3r_i r_j}{|r|^5} - \frac{\delta_{ij}}{|r|^3} \right) \right], \quad (2)$$

where γ_e and γ_I are the electron and nucleus Bohr magneton, respectively. The $\rho_s(r)$ is the spin density of the spin state of S at the position r and r_i refers to the unit vector of $i = x, y, z$. The first and second terms represent the Fermi-contact and dipole-dipole terms, respectively. The Fermi-contact term strongly depends on the spin density localized at the nucleus. We note that Eq. (2) is modified within the PAW formalism [45], and the spinpolarization of the core orbitals is considered for accurate Fermi-contact term calculations [46].

We observed that the dynamic Jahn-Teller (DJT) effect suppresses the orbital moment, at least partially, which is referred to as the Ham-reduction [47–49]. The inherent electronic λ_0 can be read directly from the scalar-relativistic spin-orbit splitting [50] of the respective e_g or e_u Kohn-Sham orbitals. The electronic spin-orbit splitting is suppressed due to DJT by the Ham reduction factor p ; thus, the observed value in experiments is $\lambda = p\lambda_0$. The value of p depends on the vibronic wavefunctions (see the derivation in Ref. 26), thus the

vibronic wavefunctions should be calculated that we implement within DJT effect. DJT also substantially affects the hyperfine tensor parameters that we derive in the Appendix (Sec. B). We show there that static hyperfine tensor calculation in the high symmetry configuration is insufficient to describe the complex physics of the vibronic Jahn–Teller states.

In our study, we explore the Jahn–Teller effect by calculating parameters for an effective single-degenerate-mode model. This model represents motion along a symmetry-breaking direction within the e_g irreducible representation, adhering to the methodology outlined in previous works [26]. Within the linear Jahn–Teller theory, the $E_g \otimes e_g$ (electronic ground state) and $E_u \otimes e_g$ (electronic excited state) APESs have a sombrero shape. The inclusion of quadratic terms disrupts the axial symmetry, resulting in three equivalent minima and saddle points [49] as illustrated in Fig. 1(d).

Below, we discuss the *ab initio* DFT analysis of the DJT effect and the respective magneto-optical properties. To address convergence issues in degenerate high-symmetry configurations and accurately determine D_{3d} symmetry geometries, we adopt a strategy involving half-half fractional occupations in half-filled degenerate orbitals within the spin-minority channel. This method simulates the ensemble of two degenerate states, effectively suppressing JT interactions and relaxing to the D_{3d} configuration. Subsequently shifting to integer occupations enables for relaxation along the e_g -symmetry direction towards the lowest energy broken-symmetry configuration [BS point in Fig. 1(d)]. This technique enables the identification of the lowest energy point, $Q_{e_g;BS}$.

For a comprehensive examination of the APES, we parameterize $\Delta Q_{e_g;BS}$ using a parameter w . In scenarios where $w = 1$, a broken symmetry configuration emerges, whereas $w = 0$ corresponds to a high-symmetry configuration. This method allows us to systematically explore the APES for $\Delta Q_{e_g;x}$ component of an effective mode, adiabatically transitioning from $w = 1.2$ to $w = 0$ to identify minima and from $w = -1.2$ to $w = 0$ to locate saddle point, thereby mitigating convergence issues associated with degeneracy close to the high-symmetry point.

However, this technique sometimes results in divergent energies as w approaches zero from positive and negative directions due to the inability of the exchange-correlation functional to yield identical energies for degenerate densities [51]. We address this issue by applying a rigid vertical shift to one of the branches, ensuring identical energies at $w = 0$.

Assuming only linear Jahn–Teller interaction, to simplify the estimation of Jahn–Teller relaxation energy E_{JT} at different pressures and to reduce the computational complexity, we develop a novel practical computational procedure that avoids issues related to degeneracy of electronic states. Since the slice cut of sombrero APES is described by $U(Q_{e_g;x}) = \omega^2 Q_{e_g;x}^2/2 - VQ_{e_g;x}$, where V is vibronic coupling constant, energy minimum is at

$\Delta Q_{e_g;BS} = V/\omega^2$, yielding Jahn–Teller relaxation energy $E_{JT} = V^2/2\omega^2$ [49]. However, by using fractional occupations described above we suppress Jahn–Teller interactions and potential energy surface attains the harmonic form $U_{ad}(Q_{gx}) = \omega^2 Q_{e_g;x}^2/2$. Plugging in the coordinate of Jahn–Teller minimum into harmonic potential we obtain $U_{ad}(\Delta Q_{e_g;BS}) = V^2/2\omega^2 \equiv E_{JT}$. This allows to estimate E_{JT} from high-symmetry and broken-symmetry geometries and one single-point calculation with fractional occupations at broken-symmetry geometry.

III. RESULTS

In this study, we characterize the G4V(–) color centers under compressive hydrostatic pressure by means of *ab initio* supercell calculations. In this context, we always mean compressive pressure in the entire study that we do not explicitly mention further on. Under hydrostatic pressure, the fundamental band gap of the diamond widens that can also shift the photoionization threshold levels of G4V defects which sets the photoionization thresholds of G4V(–) color centers. So, we compute first the charge transition levels of G4V defects to identify their photostable excitation energies assuming single photon absorption. Then we compute the ZPL energies under increasing hydrostatic pressure up to 180 GPa which gives information about the conditions of fluorescence for each G4V(–) color center at a given hydrostatic pressure. We continue the characterization of the fine level structure in the electronic ground and excited states under hydrostatic pressure. In particular, the spin-orbit splitting is determined together with hyperfine tensors for the relevant isotopes of the dopant and neighbor ^{13}C nuclear spins as well as the quadrupole moments of the relevant dopants in G4V(–) centers. These data are spectroscopy fingerprints of the G4V(–) centers under a given hydrostatic pressure. Furthermore, these data are also important in understanding the temperature-dependent electron spin coherence time of G4V(–) color centers. These spin interactions are strongly interwoven with electron-phonon interaction that we treat with Jahn–Teller theorem as we briefly described in the Method section. As a consequence, the Jahn–Teller parameters are calculated at each considered hydrostatic pressure for each G4V(–) color center at the electronic ground and excited states and will be reported before providing the fine level structure.

A. Photoionization thresholds and zero-phonon line energies

The photoionization threshold energies can be calculated from the charge transition levels referenced to the appropriate band edge. In particular, the photostability of G4V(–) is of interest. In this case, the (–|0) level with respect to the conduction band minimum (CBM)

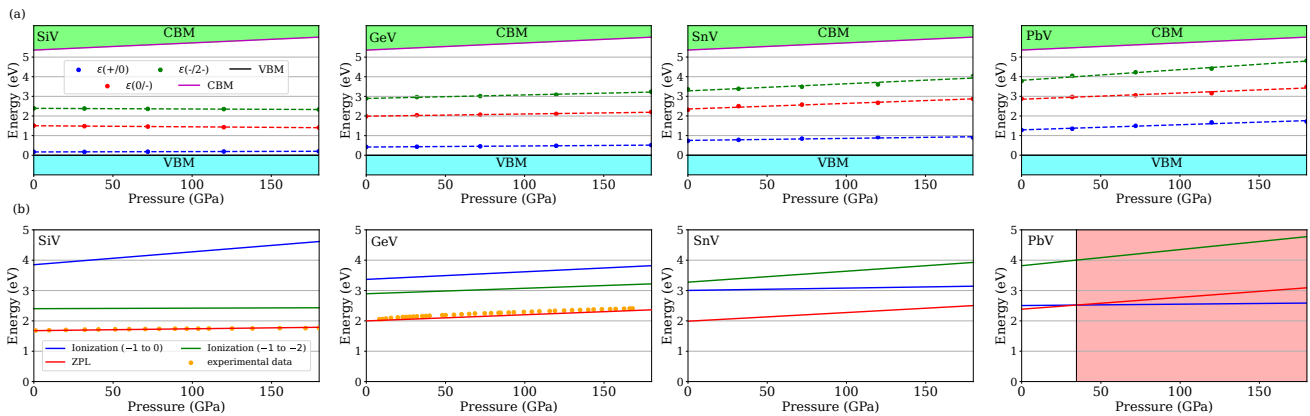


FIG. 2. (a) Calculated charge transition levels of SiV, GeV, SnV and PbV defects under hydrostatic pressure in the range of 0 to 180 GPa as obtained by HSE06 functional. (b) The ZPL shift under hydrostatic pressure was calculated by SCAN functional where the zero pressure value was aligned to the experimental data. For SiV and GeV defects the experimental data points for non-zero pressure are also given from Ref. 19. We highlight the hydrostatic pressure region by light red color where PbV(-) is not photostable.

yields the photoionization threshold for converting the negatively charged defect to neutral one, whereas the $(2 - | -)$ level with respect from the valence band maximum (VBM) yields the photoionization threshold energy for converting the negatively charged defect to doubly negative charged one. If the ZPL energy of the G4V(-) is larger than either of these photoionization threshold energies then G4V(-) is not a photostable color center.

The charge transition levels of defects can be calculated within 0.1 eV accuracy in diamond by HSE06 functional [52], thus we apply this method. The calculation methods of charge transition levels for G4V defects are given in our previous study [26] with using the standard procedure [53] that we do not reiterate here. We note that the reported values are valid at $T = 0$ K and phonon-assisted photoionization can decrease the effective thresholds at elevated temperatures (e.g., Ref. [54]).

We find that the increase of hydrostatic pressure from 0 to 180 GPa leads to the widening of the fundamental band gap of diamond by 0.66 eV. The calculated charge transition levels of G4V(-) shift upward with increasing pressure. The general trend is that the heavier the dopant ion the steeper is the upward shift in the charge transition level (Fig. 2). The same trend can be observed in the shift of ZPL. We already discussed its origin in our previous study for SiV(-) and GeV(-) color centers [19] which can be qualitatively explained through an investigation of Kohn-Sham molecular orbital states by using a single-particle picture. In the first order, the ZPL energy scales with the difference between the unoccupied and occupied states, named e_g and e_u . Thus, the change in ZPL energy upon varying hydrostatic pressures can be estimated as $E_{ZPL}(p) \propto \epsilon_u(p) - \epsilon_g(p)$, where $\epsilon_g(p)$ and $\epsilon_u(p)$ are the Kohn-Sham energies of the orbitals e_g and e_u at pressure p , respectively. The crucial distinction among the hydrostatic pressures is the deformation potential of the e_g orbital, which transitions from bonding

to antibonding as the pressure increases [55]. This applies to SnV(-) and PbV(-) color centers too. Although PbV(-) shows the most sensitive pressure dependence, this also holds to the photoionization thresholds. We find that the photoionization threshold towards CBM crosses the ZPL energies at around 32 GPa hydrostatic pressure which sets a limit for PbV(-) in pressure sensor application.

B. Dynamic Jahn-Teller effect and electron-phonon parameters

The electronic structure of the electronic ground and excited states is subject to the dynamic Jahn-Teller (DJT) effect for G4V(-) centers that was described in detail in Ref. 26 and later exploited in other studies too [15, 19, 35]. In DFT calculations, the geometry optimization yields the low C_{2h} symmetry as the global energy minimum for zero pressure but the system can be forced to stay in the high D_{3d} symmetry in the DFT calculations. In D_{3d} symmetry the distances between the three symmetrically equivalent neighbor carbon atoms are labeled by d_2 whereas the distance between the dopant ion and the nearest neighbor carbon atoms is labeled by d_1 in Fig. 1(a), and the values are listed in Table I. The general trend is that d_1 and d_2 values increase with heavier ions in G4V(-) centers at zero pressure. This may be expected as a larger ion creates a stronger strain field around the dopant ion. For a given G4V(-) center the d_1 and d_2 values slowly decrease with increasing the hydrostatic pressure. This may be also expected as the hydrostatic pressure generally decrease the bond length in the diamond crystal which also holds for the bond lengths in the center of G4V defects.

For each applied hydrostatic pressure, we calculated the APES by SCAN functional as illustrated in Fig. 1(d).

TABLE I. The structural parameters of G4V centers in D_{3d} symmetry are denoted as d_1 and d_2 as obtained by SCAN calculations. These parameters correspond to the bond length between the dopant atom and their first neighbor carbon atoms and the distances between these carbon atoms, respectively, measured in Ångström unit (Å). The d_1 and d_2 distances in the ground state at zero pressure as obtained by SCAN/HSE06 are also listed for comparison.

defect	0 GPa		180 GPa	
	d_1	d_2	d_1	d_2
ground state				
SiV(-)	1.97/1.96 ^a	2.67/2.67 ^a	1.79	2.40
GeV(-)	2.01/2.01 ^a	2.74/2.73 ^a	1.84	2.48
SnV(-)	2.09/2.08 ^a	2.83/2.83 ^a	1.92	2.58
PbV(-)	2.12/2.12 ^a	2.89/2.88 ^a	1.96	2.64
excited state				
SiV(-)	1.96	2.66	1.78	2.39
GeV(-)	2.02	2.74	1.85	2.48
SnV(-)	2.09	2.84	1.93	2.59
PbV(-)	2.15	2.91	1.98	2.66

^a Ref. 26

For the zero-pressure case, we compared the SCAN data with previous HSE06 data (see Table II). We find a good agreement between the respective SCAN data and HSE06 data for the critical JT parameters (such as the Jahn-Teller energy E_{JT} , barrier energy δ_{JT} , and the effective frequency $\hbar\omega$) so we continued the calculations with SCAN functional for non-zero pressure cases. We observe the same DJT effect under hydrostatic pressure as for the no-pressure case with resulting in C_{2h} geometry in the global energy minimum. We list the respective JT parameters for G4V(-) centers under pressure in Table IV in the Appendix.

Having these JT parameters in hand is critical in calculating the effective spin-orbit coupling as well as the effective hyperfine tensors for the respective nuclear spins proximate to the G4V defects. These will be discussed below in the next sections.

C. Effective spin-orbit splitting

We calculated the spin-orbit coupling as obtained by SCAN functional which is an essential parameter to compute the fine electronic structure of G4V(-) centers. We label this electronic spin-orbit coupling as λ_0 and is listed for each G4V(-) for the zero-pressure case in Table II. We find that the SCAN data and the previously published HSE06 λ_0 values are in good agreement for each electronic state in each G4V(-) color center. Therefore, we are convinced that the pure electronic spin-orbit coupling can be further calculated for the G4V(-) color centers under non-zero hydrostatic pressures with SCAN functional.

The electronic spin-orbit coupling is reduced due to strong electron-phonon coupling, which is often called

the Ham reduction factor that we label by p . We described the *ab initio* calculation of the Ham reduction factor for the relevant $E \otimes e$ JT system in our previous publication [56] that we applied to G4V(-) defects in a subsequent study [26]. We find for the non-zero pressure case that the calculated p factors and the resulting λ for the electronic ground and excited state of G4V(-) as obtained by SCAN and HSE06 functionals agree and they also agree with the experimental data (see Table II) as expected because both the JT parameters and the electronic spin-orbit values agree well as obtained by the respective SCAN and HSE06 functionals. We conclude that we can further apply the SCAN functional to study the hydrostatic pressure dependence of the effective spin-orbit splitting in the G4V(-) color centers.

The calculated effective spin-orbit splitting under hydrostatic pressure as obtained by SCAN functional is plotted in Fig. 3(a). The general trend is that the effective spin-orbit splitting is monotonously increasing with increasing hydrostatic pressure both in the electronic ground and excited states. The calculated effective spin-orbit splitting has two factors: the Ham-reduction parameter and the calculated electronic spin-orbit splitting (see Table IV). We find that the Ham-reduction parameter only slightly varies as a function of hydrostatic pressure, thus the inherent electronic spin-orbit splitting is dominantly increasing with raising the hydrostatic pressure. The largest contribution to the electronic spin-orbit splitting comes from the spin-orbit coupling on the dopant ion [26]. With increasing the hydrostatic pressure the distance (d_1) between the dopant ion and the neighbor carbon atoms is decreasing so the overlap of the dangling bonds with the dopant ion is increasing (see also Sec. III D). As a consequence, the wavefunction cloud around the dopant ion is denser with increasing hydrostatic pressure which contributes the most to the increasing spin-orbit coupling. The steepest shift in the effective spin-orbit splitting can be observed for SnV(-) color center.

We plot the sum of λ_g and λ_u - defined in Fig. 1(c) - as a function of the applied hydrostatic pressure in Fig. 3 that we discuss in the context of the broadening of the ZPL emission. Off-resonant excitation of G4V(-) color centers should result in emission in all the possible combinations of states and levels depicted in Fig. 1(c). By assuming a homogeneous strain field and neglecting the isotope effects (in the GHz region), the sum of λ_g and λ_u yields the width of the zero-phonon line. In experiments, the broadening of ZPL for SiV(-) varied from 10 meV to 30 meV going from zero to 180 GPa of hydrostatic pressure, whereas it varied from 15 meV to 30 meV for GeV(-), respectively [19]. In our calculations, the spin-orbit splitting related broadening of the ZPL emission varies between 1.4 meV to 1.8 meV for SiV(-) going from zero to 180 GPa of hydrostatic pressure, whereas it varies between 5.5 meV to 6.7 meV for GeV(-), respectively. The calculated values are an order of magnitude smaller

TABLE II. The calculated Jahn-Teller (JT) energy in meV (E_{JT}), the barrier energy in meV (δ_{JT}), the effective mode in meV ($\hbar\omega$), spin-orbit splitting λ_0 (meV), p reduction factor, and λ (GHz) which is Ham reduced λ_0 for the G4V(-) defects ($\lambda = p\lambda_0$) with no applied pressure. The left/right hand side data are from SCAN/HSE06 calculations.

Defects	E_{JT} (meV)	δ_{JT} (meV)	$\hbar\omega$ (meV)	λ_0 (meV)	p	λ (GHz)	λ_{exp} (GHz)
ground state							
SiV(-)	40.86 / 42.30 ^a	3.79 / 3.0 ^a	89.70 / 85.20 ^a	0.86 / 0.82 ^a	0.34 / 0.31 ^a	70.26 / 61.0 ^a	50 ^b
GeV(-)	30.59 / 30.10 ^a	4.05 / 2.0 ^a	77.01 / 82.20 ^a	2.45 / 2.20 ^a	0.38 / 0.39 ^a	222.8 / 207 ^a	181 ^c
SnV(-)	20.81 / 21.60 ^a	1.15 / 1.6 ^a	64.87 / 79.40 ^a	8.69 / 8.28 ^a	0.44 / 0.47 ^a	915.2 / 946 ^a	850 ^d
PbV(-)	15.02 / 15.60 ^a	3.88 / 0.6 ^a	51.98 / 74.90 ^a	35.0 / 34.6 ^a	0.48 / 0.54 ^a	4097 / 4514 ^a	3914 ^e
excited state							
SiV(-)	62.58 / 78.50 ^a	1.12 / 2.7 ^a	60.97 / 73.50 ^a	8.864 / 6.96 ^a	0.133 / 0.128 ^a	286.2 / 215 ^a	260 ^b
GeV(-)	71.48 / 85.70 ^a	2.31 / 5.4 ^a	70.64 / 73.00 ^a	35.03 / 36.1 ^a	0.136 / 0.113 ^a	1155 / 987 ^a	1120 ^c
SnV(-)	67.69 / 83.10 ^a	4.20 / 6.8 ^a	68.13 / 75.60 ^a	94.77 / 96.8 ^a	0.140 / 0.125 ^a	3214 / 2897 ^a	3000 ^d
PbV(-)	87.32 / 91.60 ^a	6.69 / 12.3 ^a	77.93 / 78.60 ^a	241.4 / 245 ^a	0.116 / 0.119 ^a	6782 / 7051 ^a	-

^a Ref. 26

^b Ref. 2

^c Ref. 5

^d Ref. 8

^e Ref. 18

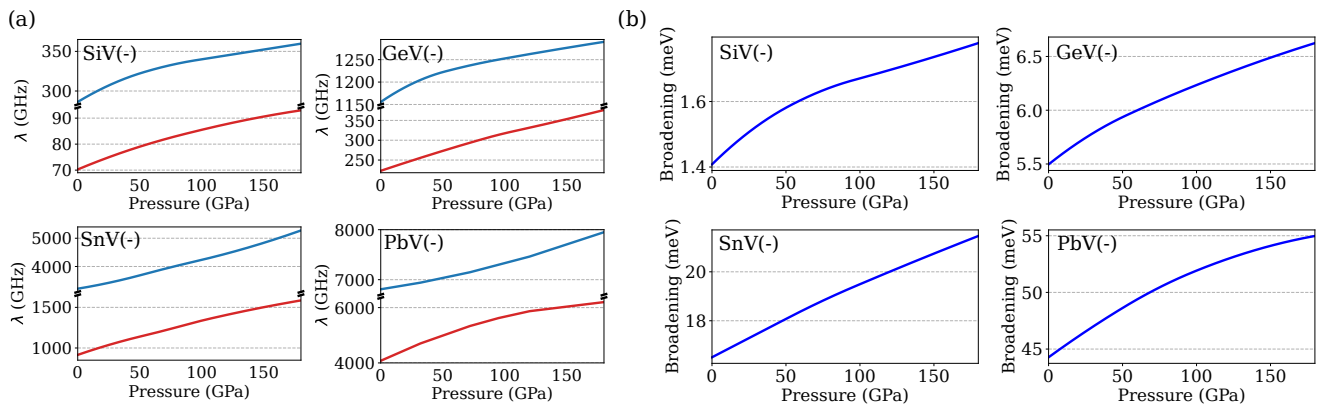


FIG. 3. (a) The SCAN calculation of hydrostatic pressure (GPa) dependence of the effective spin-orbit splitting λ in GHz unit (GHz) for G4V(-) color centers in the electronic excited and ground states plotted by blue and red lines, respectively. (b) The sum of the electronic excited and ground state's λ values associated with the zero-phonon line broadening at elevated observation temperatures with off-resonant excitation for each G4V(-) color center as a function of the applied hydrostatic pressure.

both in terms of absolute values and changes upon hydrostatic pressures. We conclude that before applying pressure to the sample, non-uniform local strain fields could be already present in the samples, which causes inhomogeneous broadening in the region of 10 meV. By applying hydrostatic pressure to the samples, it could further increase the variety of the local strain fields that may explain the observed wide broadening of the ZPL emission for SiV(-) and GeV(-) optical centers.

D. Hyperfine interaction

We computed the hyperfine tensors for the relevant isotopes of dopants and proximate ^{13}C $I = 1/2$ nuclear spins that can be basically resonantly addressed optically [30, 57]. The ^{13}C nuclear spins occur with 1.1% abundance in natural diamonds. The G4V(-) color centers are often generated by ion implantation for which the isotope can be well controlled. The non-zero nuclear spin isotopes are ^{29}Si , ^{73}Ge , ^{117}Sn and ^{207}Pb with $I = 1/2$, $I = 9/2$, $I = 1/2$, and $I = 1/2$, respectively. For ^{73}Ge

with $I = 9/2$ the quadrupole moment also contributes to the fine level structure of the $\text{GeV}(-)$ color center that we will also consider in this section. If these nuclear spins can be well controlled, then they could be applied as quantum memory of the system [23, 58] but may also contribute to extra spin flip-flop processes by reducing the coherence time of the electron spin of $\text{G4V}(-)$ centers. Therefore, understanding the full hyperfine tensor and its effects on the system is crucial in quantum technology applications. As the electronic states are dynamically distorted by phonons, such hyperfine and quadrupole matrix elements are activated that play an important role in the possible spin relaxation processes [59, 60]. In this study, we consider the full dynamical hyperfine and quadrupole tensors in the analysis of $\text{G4V}(-)$ color centers.

We start the general description of the hyperfine interaction with taking into account the ${}^2E_{g,u}$ double degenerate electronic states, which leads to dynamical terms due to strong electron-phonon coupling,

$$\hat{W} = \overleftarrow{S} \overleftarrow{A} \overrightarrow{I} + \overleftarrow{S} \overleftarrow{A}_x \overrightarrow{I} \hat{\sigma}_z + \overleftarrow{S} \overleftarrow{A}_y \overrightarrow{I} \hat{\sigma}_x \quad (3)$$

where the A is the well-known static term and A_x and A_y are the dynamic terms of the hyperfine tensor (see Appendix B and Refs. 59 and 60). The dopant ion in $\text{G4V}(-)$ center sits in the inversion point of the defect, therefore, the electron spin and nuclear spin of the system can be simultaneously diagonalized, in other words, the double group symmetry of the static hyperfine interaction remains within D_{3d} symmetry. In this case, the diagonal form of the static hyperfine tensor can be simplified to

$$\hat{H}_{\text{HF-stat}} = \frac{1}{2} A_{\perp} (\hat{S}_+ \hat{I}_- + \hat{S}_- \hat{I}_+) + A_{\parallel} \hat{S}_z \hat{I}_z, \quad (4)$$

where A_{\parallel} is parallel to the symmetry axis whereas A_{\perp} term is able to induce spin flip-flop process between the electron spin - nuclear spin states within the same orbital component. However, the electron-phonon induced hyperfine interaction should also be considered that reads as

$$\hat{H}_{\text{HF-dyn}} = A_1 \left[(\hat{S}_+ \hat{I}_z + \hat{S}_z \hat{I}_+) \hat{\sigma}_- + (\hat{S}_z \hat{I}_- + \hat{S}_- \hat{I}_z) \hat{\sigma}_+ \right] + A_2 \left[(\hat{S}_- \hat{I}_- \hat{\sigma}_- + \hat{S}_+ \hat{I}_+) \hat{\sigma}_+ \right], \quad (5)$$

where A_1 and A_2 parameters are defined in the Appendix B. It is important to highlight that A_1 and A_2 parameters are subject of the JT effect so the electronic parameters as computed within Born–Oppenheimer approximation will be reduced as explained in the Appendix B. We note that the orbital angular momentum is significantly quenched but cannot be fully neglected [26]. As a consequence, the remaining orbital angular momentum may contribute to the effective dipole-dipole hyperfine coupling. On the other hand, we assume that this contribution is small (e.g., few percents) and we do not consider it further in this context.

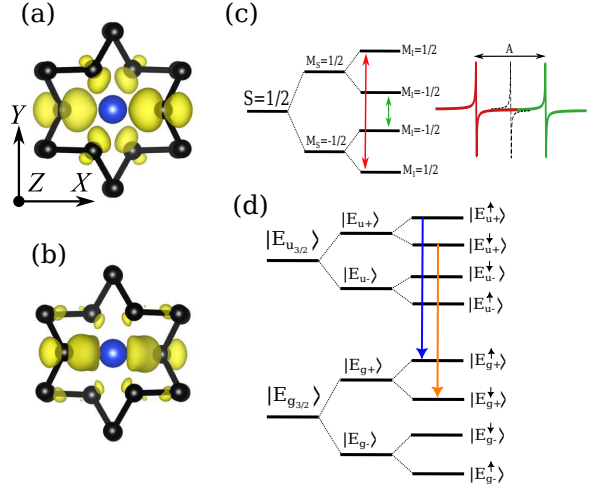


FIG. 4. The electron spin density of $\text{SiV}(-)$ center with low C_{2h} symmetry in the electronic (a) ground and (b) excited states is depicted with isosurface value of $5 \times 10^{-3} e/\text{\AA}$. (c) Scheme of the hyperfine splitting and EPR spectrum for a system with electron and nuclear spin of 1/2. (d) The possible electronic transition between two excited and ground state within the hyperfine splitting are depicted in blue and orange lines. Hence, the optical spacing A_{PLE} can be detected.

The strong electron-phonon coupling is responsible for relatively short coherence times of the electron spin in $\text{G4V}(-)$ defects even at cryogenic temperatures [61], thus no electron spin resonance measurements have been reported for $\text{G4V}(-)$ defects. The hyperfine structure may be observed by optical means. In the optical transition, the nuclear spin state does not flip thus it could be observed as an energy difference between the same m_I hyperfine levels at 2E_u (A_u) and 2E_g (A_g) which is labeled as $A_{\text{PLE}}^{\text{exp}} = 1/2(A_u - A_g)$. In the case of $I = 1/2$, two lines appear in the spectrum, which is then separated by $A_{\text{PLE}}^{\text{exp}}$. Typically, the chosen final state in the experiments is the lowest energy branch of ${}^2E_{3/2,g}$ because it has much longer coherence times than that of the upper branch. In many experiments, they resonantly excite the lower branch at ${}^2E_{3/2,u}$, so ${}^2E_{3/2,u} \rightarrow {}^2E_{3/2,g}$ optical transition occurs in the ZPL fluorescence. They typically apply relatively small magnetic fields (1.5–40 G) to split the Kramers-doublets that act as qubits: $E_{+, \uparrow, g}$ and $E_{-, \downarrow, g}$ of which levels are separated by $g_g \mu_B B$ where $g_g \approx 2$, μ_B and B are the effective g-constant, the Bohr-magneton of the electron and the strength of the applied magnetic field, and the arrows represent the electron spin projections. The nuclear Zeeman shifts can be neglected beside these terms. Within the ${}^2E_{3/2,u}$ states the effect is similar that goes with $g_u \approx 2$ effective g-constant upon external magnetic fields. At the same time, similar splitting occurs in the upper branches (${}^2E_{-, \uparrow, g/u}$ and ${}^2E_{+, \downarrow, g/u}$) (see Fig. 4).

In Table III we list the calculated hyperfine parameters of dopants for $\text{G4V}(-)$ centers. In these calculations, we use HSE06 functional in order to obtain accurate results

TABLE III. The hyperfine parameters of the G4V(-) centers as obtained by HSE06 functional in C_{2h} symmetry configuration. The $(A_{\parallel}, A_{\perp})$ and (A_1, A_2) parameters are defined in Eqs. (4) and (5), respectively, where we list here the reduced parameters with reduction factors given in Table VII. The calculated A_{PLE} values are valid at zero magnetic field as observed in the optical transition between the respective $E_{3/2,u}$ and $E_{3/2,g}$ states (see text for details). $A_{\text{PLE}}^{\text{exp}}$ data are taken with different experiments at various external magnetic fields. Our theory implies that the applied magnetic field in the range of 10-50 Gauss has less than 0.1% effect on A_{PLE} .

Nuclear	Spin	A_1 (MHz)	A_2 (MHz)	A_{\parallel} (MHz)	A_{\perp} (MHz)	A_{PLE} (MHz)	$A_{\text{PLE}}^{\text{exp}}$ (MHz)
Ground state							
^{29}Si	1/2	2.9	-3.0	83.3	88.7	-39.3	35 ^a
^{73}Ge	9/2	-0.8	0.9	41.2	44.0	-18.4	-12.5(5) ^b
^{117}Sn	1/2	-1.1	0.9	976.0	1029.7	-473.05	-484(8) ^b
^{207}Pb	1/2	1.6	0.5	-1149.4	-1192.0	565.0	-
Excited state							
^{29}Si	1/2	0.03	-0.01	4.8	5.1	-	-
^{73}Ge	9/2	-0.22	0.26	4.5	4.6	-	-
^{117}Sn	1/2	-0.1	-0.2	29.9	32.3	-	-
^{207}Pb	1/2	-0.06	0.4	-19.4	-20.76	-	-

^a Ref. 62

^b Ref. 35

for the spin density near the nuclear spins. We find that the spin density cloud around the dopant ion is less dense in the electronic excited state than that in the electronic ground state in each G4V(-) color center. As a consequence, the static hyperfine parameters of dopant ion are larger in the electronic ground state than that in the electronic excited state. As a consequence, the hyperfine lines for $I > 0$ dopants can be indeed observed because A_{PLE} becomes non-zero.

It can be also seen that the dynamic hyperfine parameters are small but non-zero in both 2E_u and 2E_g states as listed in Table III. The A_1 represents the degree of bending of spin density from the XY plane towards the Z -direction (out of plane), whereas A_2 denotes the intensity of rotation of the π orbital within the XY plane. Thus, A_1 and A_2 parameters are nearly zero for both the ground and excited states due to minimal participation of π orbital and the bending spin density out of the XY plane (Fig. 4(a, b)).

In the relevant $^2E_{3/2,g/u}$ states split by the external magnetic field, the A_1 hyperfine interaction mixes $E_{-, \downarrow, g/u}$ with $E_{+, \uparrow, g/u}$. Since $|A_{\parallel}| \gg |A_1|$ and by assuming a positive magnetic field aligned to the symmetry axis of the defect the hyperfine splitting in the lowest energy branch can be approximated as

$$A_{g/u} = A_{\parallel, g/u} + \frac{A_{1, g/u}^2}{g_{g/u} \mu_B B + A_{\parallel, g/u}}, \quad (6)$$

so the actual hyperfine splitting will be weakly magnetic field dependent because of dynamic hyperfine mixing of

E_+ and E_- orbitals. As a consequence, the optical transition between hyperfine lines will be also weakly magnetic field dependent: the larger the magnetic field is then the mixing term is more suppressed. By comparing the experimental data and our theory about hyperfine-related splitting in the optical transition we find good agreement. We conclude that the hyperfine couplings are accurately calculated with our method at zero pressure. The hyperfine parameters in the ground and excited states cannot be directly observed in quantum optics measurements so our data can be used for analyzing G4V(-) color centers. We provide further hyperfine data about proximate ^{13}C nuclear spins. These nuclear spins do not reside in the symmetry axis therefore the static and dynamic hyperfine tensors have to be derived for such cases that we present in Appendix B. The results are listed in Table VII. We also studied the quadrupole moment of Ge isotope with $I = 9/2$ nuclear spin in GeV(-) for which the dynamical $Q_{1,2}$ may flip the nuclear spin as explained in Refs. [59, 60]. The quadrupole moment (Q) can be calculated as

$$Q = \frac{\rho e^2 V_{ZZ}}{h} \quad (7)$$

where ρ is the nuclear quadrupole moment, e is the elementary charge, V_{ZZ} is the electric field gradient (EFG) at the nucleus site and h is Planck's constant [63]. With using $\rho = -196 \times 10^{-31} m^2$ (Ref. 64) we obtained $Q = -13.4$ MHz, $Q_1 = -11.5$ MHz and $Q_2 = -10.3$ MHz.

As a next step, we computed the pressure dependence of the hyperfine parameters. For the sake of simplicity,

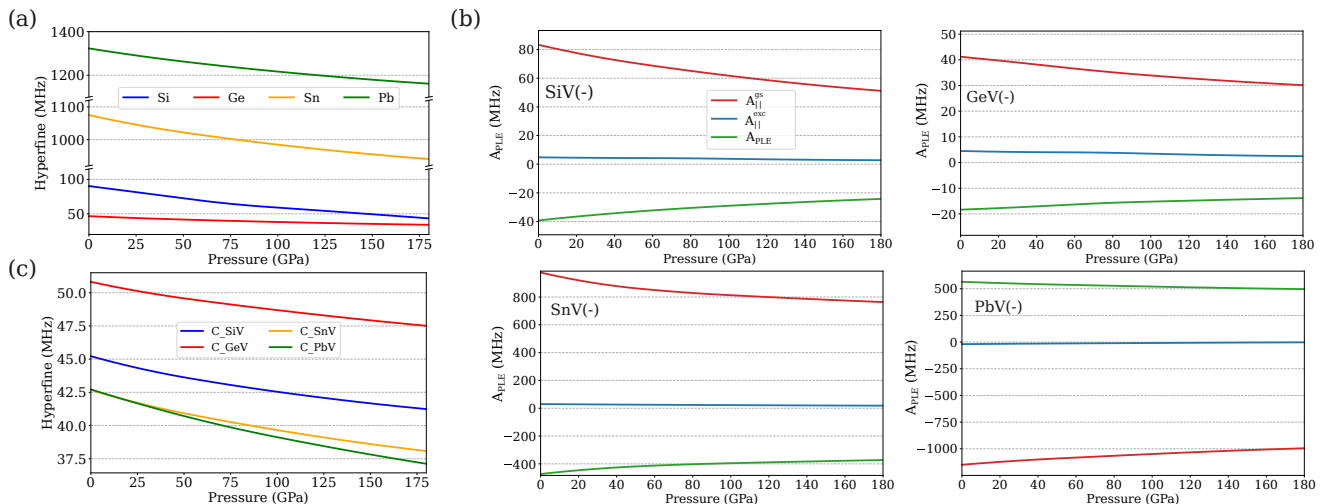


FIG. 5. Absolute value of the Fermi-contact hyperfine constants in $G4V(-)$ centers as obtained with HSE06 functional as a function of hydrostatic pressure for (a) dopant atoms and (c) first neighbor carbon atoms. These calculations were carried out in D_{3d} symmetry configurations. (b) The illustration of A_{PLE} , A_{\parallel}^{gs} and A_{\parallel}^{exc} as a function of hydrostatic pressure for dopant atoms (see text for details) with low C_{2h} point group symmetry. The plots were fit to quadratic functions.

we plot the absolute value of the Fermi-contact hyperfine constant for the dopants and the nearest neighbor ^{13}C nuclear spins as a function of the applied hydrostatic pressure in Figs. 5(a,b). We find that the hyperfine constants are generally decreasing with increasing hydrostatic pressures in the electronic ground state because the spin density is less localized with increasing hydrostatic pressures (see Fig. 6). We also find that the heavier the dopant the larger the change in the hyperfine constant on the dopant ion upon hydrostatic pressure. We also plot the computed A_{PLE} under hydrostatic pressure which can be directly observed in quantum optics measurements. We find that the absolute values of A_{PLE} also reduces with increasing hydrostatic pressure because the absolute value of the hyperfine constants reduces much faster in the electronic ground state than that in the electronic excited state.

IV. SUMMARY

In this work, we studied the pressure-dependent magneto-optical spectrum of $G4V$ centers while assuming compressive hydrostatic pressures by means of plane wave supercell density functional theory calculations. We showed that the strong electron-phonon coupling significantly modifies the electronic spin-orbit, quadrupole and hyperfine interactions. In particular, we developed a theory for calculating the effective hyperfine tensors for $E \otimes e$ Jahn-Teller systems and applied it to the $G4V$ centers. We find that all these parameters shift with hydrostatic pressures and cross-correlation measurements of these parameters may be applied to deduce the external hydrostatic pressures. We find that the maximum pressure

is set at about 32 GPa for $\text{PbV}(-)$ center based pressure sensor because the photostability of $\text{PbV}(-)$ is compromised at larger pressures.

ACKNOWLEDGEMENT

This work was supported by the Hungarian National Research, Development and Innovation Office (NKFIH) for Quantum Information National Laboratory of Hungary (grant no. 2022-2.1.1-NL-2022-00004), the EU QuantERA II Sensxtreme project (NKFIH grant no. 2019-2.1.7-ERA-NET-2022-00040), the Horizon Europe EIC Pathfinder QuMicro project (grant no. 101046911) and SPINUS project (grant no. 101135699).

Appendix A: Additional data for the effective spin-orbit splitting

Here, we list the calculated Jahn-Teller parameters and electronic spin-orbit splitting under compressive hydrostatic pressure as obtained by SCAN functional for $G4V(-)$ color centers.

Appendix B: Hyperfine tensors under dynamic Jahn-Teller interaction

The hyperfine tensor elements can be evaluated by spinpolarized DFT whenever the $|e_x\rangle$ or $|e_y\rangle$ orbital is being occupied for defects exhibiting D_{3d} symmetry. In simple words, the hyperfine tensor elements can be evaluated whenever $|e_x\rangle$ or $|e_y\rangle$ state is being selected. There-

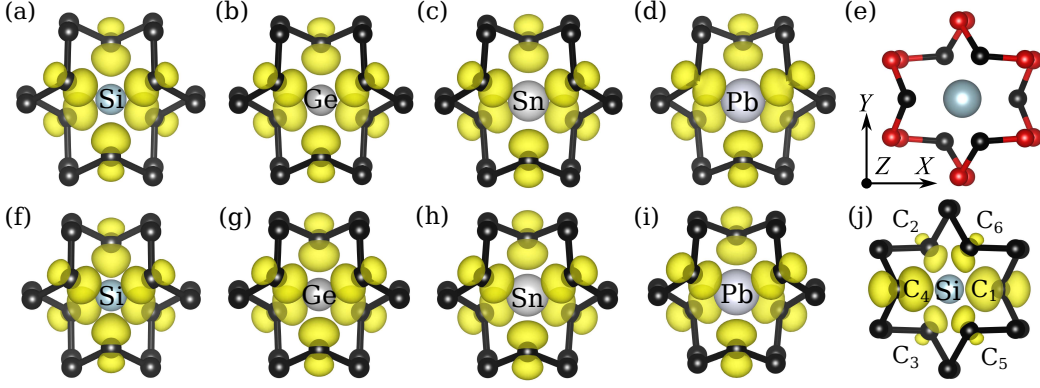


FIG. 6. Illustration of the spin density in D_{3d} symmetry. (a) SiV(-), (b) GeV(-), (c) SnV(-), and (d) PbV(-) defects with zero pressure and (f) SiV(-), (g) GeV(-), (h) SnV(-), and (i) PbV(-) defects under 180 GPa hydrostatic pressure. (e) The scheme of first and second carbon neighbor atoms in black and red spheres, respectively. (j) The spin density of SiV(-) which is representative of all G4V centers in C_{2h} symmetry with no pressure. The electron spin density is depicted with an isosurface value of $5 \times 10^{-3} e/\text{\AA}$.

TABLE IV. The SCAN calculated ground and excited states of Jahn-Teller (JT) energy in meV (E_{JT}), the barrier energy in meV (δ_{JT}), the effective mode in meV ($\hbar\omega$), p reduction factor, and λ (GHz) which is Ham reduced spin-orbit splitting for the G4V(-) defects with hydrostatic pressure.

Pressure (GPa)	Ground states					Excited states				
	E_{JT} (meV)	δ_{JT} (meV)	$\hbar\omega$ (meV)	p	λ (GHz)	E_{JT} (meV)	δ_{JT} (meV)	$\hbar\omega$ (meV)	p	λ (GHz)
SiV(-)										
0	40.86	3.79	89.70	0.34	70.26	62.58	60.81	1.12	0.133	286.21
32	39.62	3.08	88.97	0.34	76.15	58.57	59.16	1.32	0.141	311.82
72	38.47	2.97	87.68	0.35	82.12	56.69	58.08	1.6	0.144	331.62
120	38.72	2.55	88.18	0.35	87.71	56.61	58.00	1.71	0.144	344.89
180	39.58	2.24	89.43	0.35	93.01	56.42	58.08	1.78	0.145	359.72
GeV(-)										
0	30.59	4.05	77.01	0.38	222.84	71.48	70.49	2.31	0.136	1155.54
32	30.00	3.34	76.71	0.38	255.53	68.28	68.97	2.48	0.141	1204.69
72	29.18	3.34	75.59	0.38	293.72	65.70	67.95	2.65	0.146	1237.21
120	29.89	2.99	76.29	0.38	331.61	63.42	66.82	2.91	0.150	1262.39
180	30.82	2.56	78.36	0.38	376.21	62.18	67.03	3.2	0.155	1289.74
SnV(-)										
0	20.81	1.15	64.87	0.44	915.23	67.69	68.04	4.2	0.140	3214.51
32	20.47	1.10	64.94	0.44	1068.02	65.01	66.92	4.31	0.145	3490.44
72	20.58	1.09	64.54	0.44	1223.62	61.93	65.24	4.51	0.150	3938.52
120	21.17	0.36	66.08	0.44	1407.08	57.01	62.86	4.53	0.160	4456.48
180	22.08	0.29	67.54	0.43	1585.59	50.53	59.25	4.72	0.174	5275.23
PbV(-)										
0	15.02	3.88	55.98	0.48	4436.03	87.32	77.85	6.69	0.116	6782.56
32	15.12	3.98	56.43	0.48	5064.64	87.28	77.82	6.59	0.116	6973.45
72	15.27	3.90	56.13	0.48	5743.95	87.20	78.16	6.2	0.117	7170.19
120	16.49	3.89	59.04	0.47	6387.39	86.21	77.67	6.12	0.118	7417.08
180	18.27	4.43	55.94	0.46	6592.98	82.25	74.88	5.87	0.120	7964.79

fore, the hyperfine interaction depicted in $\hat{H}_{\text{HF}} = \hat{S}\hat{A}\hat{I}$ can be extended for orbital degrees of freedom as

$$\hat{W} = \overleftarrow{S} \overleftarrow{A}^{(xx)} \overrightarrow{I} |e_x\rangle \langle e_x| + \overleftarrow{S} \overleftarrow{A}^{(xy)} \overrightarrow{I} |e_x\rangle \langle e_y| + \overleftarrow{S} \overleftarrow{A}^{(yx)} \overrightarrow{I} |e_y\rangle \langle e_x| + \overleftarrow{S} \overleftarrow{A}^{(yy)} \overrightarrow{I} |e_y\rangle \langle e_y|, \quad (\text{B1})$$

where $\overleftarrow{A}^{(xx)}$ and $\overleftarrow{A}^{(yy)}$ tensors can be determined by applying Eq. (2) upon spin densities of $|e_x\rangle$ and $|e_y\rangle$, respectively. However, $\overleftarrow{A}^{(xy)}$, $\overleftarrow{A}^{(yx)}$ offdiagonal terms cannot be computed directly. Therefore, we will utilize D_{3d} symmetry constraints to deduce those non-trivial orbital flipping terms.

First, we introduce Pauli matrices ($\hat{\sigma}_x = \begin{pmatrix} 1 & \\ & -1 \end{pmatrix} = |e_x\rangle\langle e_y| + |e_y\rangle\langle e_x|$, $\hat{\sigma}_y = \begin{pmatrix} & -i \\ i & \end{pmatrix}$, $\hat{\sigma}_z = \begin{pmatrix} 1 & \\ & -1 \end{pmatrix} = |e_x\rangle\langle e_x| - |e_y\rangle\langle e_y|$) for orbital degrees of freedom and thus Eq. (B1) can be transformed into a compact form as

$$\hat{W} = \overleftarrow{S} \overleftarrow{A} \overleftarrow{I} + \overleftarrow{S} \overleftarrow{A}_x \overleftarrow{I} \hat{\sigma}_z + \overleftarrow{S} \overleftarrow{A}_y \overleftarrow{I} \hat{\sigma}_x + \underbrace{\overleftarrow{S} \overleftarrow{A}_z \overleftarrow{I} i \hat{\sigma}_y}_{=0} \quad (\text{B2})$$

by introducing the following hyperfine tensors as

$$\overleftarrow{A} = \frac{1}{2} \left(\overleftarrow{A}^{(xx)} + \overleftarrow{A}^{(yy)} \right) \quad (\text{B3a})$$

$$\overleftarrow{A}_x = \frac{1}{2} \left(\overleftarrow{A}^{(xx)} - \overleftarrow{A}^{(yy)} \right) \quad (\text{B3b})$$

$$\overleftarrow{A}_y = \frac{1}{2} \left(\overleftarrow{A}^{(xy)} + \overleftarrow{A}^{(yx)} \right) \quad (\text{B3c})$$

$$\overleftarrow{A}_z = \frac{1}{2} \left(\overleftarrow{A}^{(xy)} - \overleftarrow{A}^{(yx)} \right) = 0, \quad (\text{B3d})$$

where \overleftarrow{A}_z is zero because hyperfine interaction is real-valued thus symmetric.

Next, we discuss how to calculate these hyperfine interactions in practice within spinpolarized DFT calculations. In the usual Born-Oppenheimer *ab initio* DFT calculations, the double degenerate e_g orbital is occupied by a single electron in the ground state for G4V(-) defect. We analyze the system by assuming $e_{g(x)}$ is occupied by an electron in D_{3d} symmetry configuration. Among the six equivalent immediate carbon neighbor atoms together with inversion symmetry, two pairs of three carbon atoms can be rotated to each other about the C_3 symmetry axis (see Fig. 7), e.g., C_1 , C_2 , C_3 carbon atoms exhibit $\overleftarrow{A}^{(xx)}$, $\overleftarrow{B}^{(xx)}$, $\overleftarrow{C}^{(xx)}$ hyperfine tensors, respectively. In this example, we define the following hyperfine matrices for C_1 ,

$$\overleftarrow{A}^{(xx)} = \overleftarrow{A}^{(0^\circ)} = \langle +1; 0 | \hat{W} | +1; 0 \rangle = \overleftarrow{A} + \overleftarrow{A}_x. \quad (\text{B4})$$

The hyperfine tensors of C_2 and C_3 can be rotated to that of C_1 by $\pm 120^\circ$ rotations as

$$\begin{aligned} \hat{C}_3 \overleftarrow{B}^{(xx)} &= \overleftarrow{A}^{(+120^\circ)} = \left\langle -\frac{1}{2}; -\frac{\sqrt{3}}{2} \left| \hat{W} \right| -\frac{1}{2}; -\frac{\sqrt{3}}{2} \right\rangle \\ &= \overleftarrow{A} - \frac{1}{2} \overleftarrow{A}_x + \frac{\sqrt{3}}{2} \overleftarrow{A}_y, \end{aligned} \quad (\text{B5a})$$

$$\begin{aligned} \hat{C}_3^{-1} \overleftarrow{C}^{(xx)} &= \overleftarrow{A}^{(-120^\circ)} = \left\langle -\frac{1}{2}; +\frac{\sqrt{3}}{2} \left| \hat{W} \right| -\frac{1}{2}; +\frac{\sqrt{3}}{2} \right\rangle \\ &= \overleftarrow{A} - \frac{1}{2} \overleftarrow{A}_x - \frac{\sqrt{3}}{2} \overleftarrow{A}_y. \end{aligned} \quad (\text{B5b})$$

At first glance, $\hat{C}_3 \overleftarrow{B}^{(xx)}$ and $\hat{C}_3^{-1} \overleftarrow{C}^{(xx)}$ matrices should agree with $A^{(xx)}$ of C_1 . However, the rotation also acts on the orbitals thus the hyperfine tensor should be evaluated $\frac{q\eta}{A} |e_{(\pm 120^\circ)}\rangle = \frac{1}{2} |e_x\rangle \pm \frac{\sqrt{3}}{2} |e_y\rangle$ orbitals that we label as $\overleftarrow{A}^{(\pm 120^\circ)}$. Eqs. (B4)-(B5a)-(B5b) allow us to determine the orbital flipping matrices directly as

$$\overleftarrow{A} = \frac{1}{3} \left(\overleftarrow{A}^{(xx)} + \hat{C}_3 \overleftarrow{B}^{(xx)} + \hat{C}_3^{-1} \overleftarrow{C}^{(xx)} \right), \quad (\text{B6a})$$

$$\overleftarrow{A}_x = \frac{q}{4} \left(2 \overleftarrow{A}^{(xx)} - \hat{C}_3 \overleftarrow{B}^{(xx)} - \hat{C}_3^{-1} \overleftarrow{C}^{(xx)} \right), \quad (\text{B6b})$$

$$\overleftarrow{A}_y = \frac{q}{\sqrt{3}} \left(\hat{C}_3 \overleftarrow{B}^{(xx)} - \hat{C}_3^{-1} \overleftarrow{C}^{(xx)} \right), \quad (\text{B6c})$$

where we also included the effect of $q = (1+p)/2$ vibronic reduction factor [48, 49] that partially quenches the strength of $\{\hat{\sigma}_z, \hat{\sigma}_x\}$ orbital operators transforming as E representation of D_{3d} . The p reduction factor reduces the orbital operators transforming as A_2 such as $\hat{L}_z = \hat{\sigma}_y$ of Eq. (II). We note that the \overleftarrow{A} tensor can be evaluated by putting two half electrons on $|e_x\rangle$ and $|e_y\rangle$ orbitals which method was already used in Ref. 35. Finally, \overleftarrow{A}_x and \overleftarrow{A}_y are not independent for the central atom in the inversion center. Therefore, the dopant atom's hyperfine tensor can be represented by four hyperfine parameters, $A_{\parallel, \perp, 1, 2}$ that can be given [60] as

$$\begin{aligned} \hat{W} &= A_{\parallel} \hat{S}_z \hat{I}_z + A_{\perp} \left(\hat{S}_x \hat{I}_x + \hat{S}_y \hat{I}_y \right) + \\ &A_1 \left[(\hat{S}_x \hat{I}_z + \hat{S}_z \hat{I}_x) \hat{\sigma}_z + (\hat{S}_y \hat{I}_z + \hat{S}_z \hat{I}_y) \hat{\sigma}_x \right] + \\ &A_2 \left[(\hat{S}_y \hat{I}_y - \hat{S}_x \hat{I}_x) \hat{\sigma}_z + (\hat{S}_x \hat{I}_y + \hat{S}_y \hat{I}_x) \hat{\sigma}_x \right]. \end{aligned} \quad (\text{B7})$$

This equation can be rewritten with the definition $\sigma_{\pm} = \langle e_{\mp} | e_{\pm} \rangle$ and the usual ladder operators which then reads as

$$\begin{aligned} \hat{W} &= A_{\parallel} \hat{S}_z \hat{I}_z + \frac{1}{2} A_{\perp} \left(\hat{S}_+ \hat{I}_- + \hat{S}_- \hat{I}_+ \right) + \\ &A_1 \left[(\hat{S}_+ \hat{I}_z + \hat{S}_z \hat{I}_+) \hat{\sigma}_- + (\hat{S}_z \hat{I}_- + \hat{S}_- \hat{I}_z) \hat{\sigma}_+ \right] + \\ &A_2 \left[(\hat{S}_- \hat{I}_- \hat{\sigma}_- + \hat{S}_+ \hat{I}_+) \hat{\sigma}_+ \right]. \end{aligned} \quad (\text{B8})$$

Finally, we list of the electronic hyperfine tensor data in Table V as obtained in HSE06 calculations that we list for the sake of reproduction of our results and the derived hyperfine tensor data in Tables VII and III. We note that the hyperfine constants of the second neighbor atoms are almost negligible in the electronic excited state.

[1] V. S. Vavilov and A. Gippius, Sov. Phys. Semicond. 14, 1078 (1980).

[2] C. Hepp, T. Müller, V. Waselowski, J. N. Becker, B. Pin-

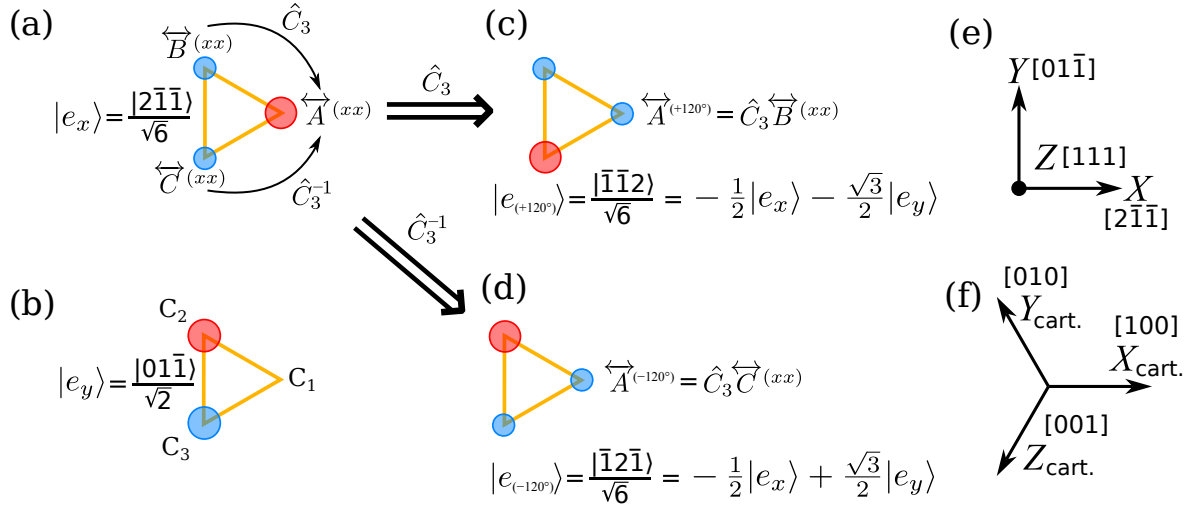


FIG. 7. Transformation of three equivalent carbon atoms. (a) and (b) represent the electronic wavefunction when the $|e_x\rangle$ and $|e_y\rangle$ are chosen, respectively. The red and blue circles represent the positive and negative values of $|e_x\rangle$ and $|e_y\rangle$ wavefunctions, respectively that we also quantify inside the [...] parentheses. (c) and (d) depict the transformation laws for \hat{C}_3 and \hat{C}_3^{-1} rotations, respectively. (e) depicts the $Z=[111]$ oriented coordinates of the G4V defects. (f) depicts the Cartesian coordinates of diamond.

- gault, H. Sternschulte, D. Steinmüller-Nethl, A. Gali, J. R. Maze, M. Atatüre, and C. Becher, *Phys. Rev. Lett.* **112**, 036405 (2014).
- [3] T. Müller, C. Hepp, B. Pingault, E. Neu, S. Gsell, M. Schreck, H. Sternschulte, D. Steinmüller-Nethl, C. Becher, and M. Atatüre, *Nature Communications* **5**, 3328 (2014).
- [4] L. J. Rogers, K. D. Jahnke, M. W. Doherty, A. Dietrich, L. P. McGuinness, C. Müller, T. Teraji, H. Sumiya, J. Isoya, N. B. Manson, and F. Jelezko, *Phys. Rev. B* **89**, 235101 (2014).
- [5] E. A. Ekimov, S. G. Lyapin, K. N. Boldyrev, M. V. Kondrin, R. Khmel'nitskiy, V. A. Gavva, T. V. Kotereva, and M. N. Popova, *JETP Letters* **102**, 701 (2015).
- [6] T. Iwasaki, F. Ishibashi, Y. Miyamoto, Y. Doi, S. Kobayashi, T. Miyazaki, K. Tahara, K. D. Jahnke, L. J. Rogers, B. Naydenov, F. Jelezko, S. Yamasaki, S. Nagamachi, T. Inubushi, N. Mizuochi, and M. Hatano, *Scientific Reports* **5**, 12882 (2015).
- [7] T. Iwasaki, Y. Miyamoto, T. Taniguchi, P. Siyushev, M. H. Metsch, F. Jelezko, and M. Hatano, *Phys. Rev. Lett.* **119**, 253601 (2017).
- [8] T. Iwasaki, Y. Miyamoto, T. Taniguchi, P. Siyushev, M. H. Metsch, F. Jelezko, and M. Hatano, *Phys. Rev. Lett.* **119**, 253601 (2017).
- [9] S. Meesala, Y.-I. Sohn, B. Pingault, L. Shao, H. A. Atikian, J. Holzgrafe, M. Gündoğan, C. Stavarakas, A. Sipahigil, C. Chia, R. Evans, M. J. Burek, M. Zhang, L. Wu, J. L. Pacheco, J. Abraham, E. Bielejec, M. D. Lukin, M. Atatüre, and M. Lončar, *Phys. Rev. B* **97**, 205444 (2018).
- [10] S. Ditalia Tchernij, T. Lühmann, T. Herzig, J. Küpper, A. Damin, S. Santonocito, M. Signorile, P. Traina, E. Moreva, F. Celegato, S. Pezzagna, I. P. Degiovanni, P. Olivero, M. Jakšić, J. Meijer, P. M. Genovese, and J. Forneris, *ACS Photonics* **5**, 4864 (2018).
- [11] M. E. Trusheim, N. H. Wan, K. C. Chen, C. J. Ciccarino, J. Flick, R. Sundararaman, G. Malladi, E. Bersin, M. Walsh, B. Lienhard, H. Bakhru, P. Narang, and D. Englund, *Phys. Rev. B* **99**, 075430 (2019).
- [12] D. Chen, N. I. Zheludev, and W. Gao, *Advanced Quantum Technologies* **3** (2019).
- [13] M. E. Trusheim, B. Pingault, N. H. Wan, M. Gündoğan, L. De Santis, R. Debroux, D. Gangloff, C. Purser, K. C. Chen, M. Walsh, J. J. Rose, J. N. Becker, B. Lienhard, E. Bersin, I. Paradeisanos, G. Wang, D. Lyzwa, A. R.-P. Montblanch, G. Malladi, H. Bakhru, A. C. Ferrari, I. A. Walmsley, M. Atatüre, and D. Englund, *Phys. Rev. Lett.* **124**, 023602 (2020).
- [14] J. Görlitz, D. Herrmann, G. Thiering, P. Fuchs, M. Gandil, T. Iwasaki, T. Taniguchi, M. Kieschnick, J. Meijer, M. Hatano, A. Gali, and C. Becher, *New Journal of Physics* **22**, 013048 (2020).
- [15] V. S. Krivobok, E. A. Ekimov, S. G. Lyapin, S. N. Nikolaev, Y. A. Skakov, A. A. Razgulov, and M. V. Kondrin, *Phys. Rev. B* **101**, 144103 (2020).
- [16] A. E. Rugar, S. Aghaeimeibodi, D. Riedel, C. Dory, H. Lu, P. J. McQuade, Z.-X. Shen, N. A. Melosh, and J. Vučković, *Phys. Rev. X* **11**, 031021 (2021).
- [17] S. Aghaeimeibodi, D. Riedel, A. E. Rugar, C. Dory, and J. Vučković, *Phys. Rev. Appl.* **15**, 064010 (2021).
- [18] P. Wang, T. Taniguchi, Y. Miyamoto, M. Hatano, and T. Iwasaki, *ACS Photonics* **8**, 2947 (2021).
- [19] B. Vindolet, M.-P. Adam, L. Toraille, M. Chipaux, A. Hilberer, G. Dupuy, L. Razinkovas, A. Alkauskas, G. Thiering, A. Gali, M. De Feudis, M. W. Ngandeu Ngambou, J. Achard, A. Tallaire, M. Schmidt, C. Becher, and J.-F. Roch, *Phys. Rev. B* **106**, 214109 (2022).
- [20] P. Wang, L. Kazak, K. Senkalla, P. Siyushev, R. Abe, T. Taniguchi, S. Onoda, H. Kato, T. Makino, M. Hatano, F. Jelezko, and T. Iwasaki, *Phys. Rev. Lett.* **132**, 073601 (2024).
- [21] M. K. Bhaskar, R. Riedinger, B. Machielse, D. S. Levo-

TABLE V. The raw data of hyperfine tensors in both D_{3d} and C_{2h} symmetries for G4V(-) defects at zero pressure as obtained in HSE06 calculations in the electronic ground state. A_{xx} , A_{yy} and A_{zz} are the symmetric hyperfine tensor elements. A_{xy} , A_{xz} and A_{yz} parameters are the asymmetric hyperfine tensor elements. The unitless reduction factor q is given for each defect associated with the Jahn–Teller effect. Atoms are labeled for low C_{2h} symmetry configuration in Fig. 6(j) and the spin density of high D_{3d} symmetry configuration is illustrated in Fig. 6.

Defect	q	A_{xx} (MHz)	A_{yy} (MHz)	A_{zz} (MHz)	A_{xy} (MHz)	A_{xz} (MHz)	A_{yz} (MHz)
SiV(-)	0.67						
C_{2h}							
$C_{2,3,5,6}$		18.36	22.91	21.14	6.03	-5.17	-7.53
$C_{1,4}$		98.46	100.94	98.45	-28.79	28.26	-28.79
^{29}Si		87.08	85.48	87.09	-4.27	3.15	-4.25
D_{3d}							
C-first neighbor		44.85	44.85	45.95	13.02	-13.41	-13.41
C-second neighbor		-2.60	-1.87	-3.32	-1.60	0.03	0.47
^{29}Si		90.29	90.29	90.29	-1.70	-1.70	-1.70
GeV(-)	0.69						
C_{2h}							
$C_{2,3,5,6}$		19.76	23.84	22.14	6.69	-5.83	-7.92
$C_{1,4}$		113.87	112.83	81.39	-31.78	31.75	-31.79
^{73}Ge		43.24	42.84	43.24	-1.63	0.45	-1.64
D_{3d}							
C-first neighbor		50.64	50.64	51.17	14.74	-14.87	-14.87
C-second neighbor		-3.91	-4.30	-3.13	0.11	-1.22	0.51
^{73}Ge		46.61	46.61	46.61	-0.93	-0.93	-0.93
SnV(-)	0.72						
C_{2h}							
$C_{2,3,5,6}$		16.32	20.34	18.48	7.13	-6.23	-8.33
$C_{1,4}$		95.15	95.64	95.16	-32.49	32.50	-32.49
^{117}Sn		1012.14	1011.20	1012.15	-18.766	-16.214	-18.763
D_{3d}							
C-first neighbor		42.61	42.61	42.84	15.40	-15.50	-15.50
C-second neighbor		-9.59	-9.85	-9.59	0.05	0.97	0.05
^{117}Sn		1074.989	1074.985	1074.99	-18.066	-18.066	-18.062
PbV(-)	0.74						
C_{2h}							
$C_{2,3,5,6}$		14.83	18.50	16.65	7.15	-6.23	-8.20
$C_{1,4}$		99.96	99.02	99.96	-33.97	34.53	-33.97
^{207}Pb		-1179.04	-1175.31	-1179.05	14.46	13.63	14.45
D_{3d}							
C-first neighbor		42.83	42.83	42.51	16.21	-16.08	-16.08
C-second neighbor		-12.13	-10.79	-11.97	0.30	-0.06	-1.26
^{207}Pb		-1323.24	-1323.24	-1323.24	14.27	14.27	14.27

nian, C. T. Nguyen, E. N. Knall, H. Park, D. Englund, M. Lončar, D. D. Sukachev, and M. D. Lukin, *Nature* **580**, 60 (2020).

[22] E. Bersin, M. Sutula, Y. Q. Huan, A. Suleymanzade, D. R. Assumpcao, Y.-C. Wei, P.-J. Stas, C. M. Knaut, E. N. Knall, C. Langrock, N. Sinclair, R. Murphy, R. Riedinger, M. Yeh, C. Xin, S. Bandyopadhyay, D. D.

Sukachev, B. Machielse, D. S. Levonian, M. K. Bhaskar, S. Hamilton, H. Park, M. Lončar, M. M. Fejer, P. B. Dixon, D. R. Englund, and M. D. Lukin, *PRX Quantum* **5**, 010303 (2024).

[23] C. M. Knaut, A. Suleymanzade, Y.-C. Wei, D. R. Assumpcao, P.-J. Stas, Y. Q. Huan, B. Machielse, E. N. Knall, M. Sutula, G. Baranes, N. Sinclair, C. De-

TABLE VI. The raw data of hyperfine tensors in both D_{3d} and C_{2h} symmetries for G4V(−) defects at zero pressure as obtained in HSE06 calculations in the electronic excited state. A_{xx} , A_{yy} and A_{zz} are the symmetric hyperfine tensor elements. A_{xy} , A_{xz} and A_{yz} parameters are the asymmetric hyperfine tensor elements. The unitless reduction factor q is given for each defect associated with the Jahn–Teller effect. Atoms are labeled for low C_{2h} symmetry configuration in Fig. 6(j) and the spin density of high D_{3d} symmetry configuration is illustrated in Fig. 6.

Defect	q	A_{xx} (MHz)	A_{yy} (MHz)	A_{zz} (MHz)	A_{xy} (MHz)	A_{xz} (MHz)	A_{yz} (MHz)
SiV(−)							
C_{2h}							
$C_{1,4}$		40.72	37.07	36.95	22.24	22.32	53.44
$C_{2,3,5,6}$		21.48	14.03	14.38	13.83	14.45	17.54
^{29}Si	0.57	4.97	5.02	4.96	4.91	4.86	4.90
D_{3d}							
C-first neighbor		−16.09	−16.09	−20.87	−14.94	−17.57	−17.57
^{29}Si		36.21	36.21	36.21	36.19	36.19	36.19
GeV(−)							
C_{2h}							
$C_{1,4}$		−8.57	−8.57	−9.73	−10.30	−8.50	−8.50
$C_{2,3,5,6}$		5.39	3.91	−1.21	−10.82	13.54	−6.84
^{73}Ge		4.59	4.51	4.59	4.28	5.01	4.28
D_{3d}							
C-first neighbor		2.91	2.91	2.42	3.01	2.44	2.44
^{73}Ge		15.437	15.912	15.439	−0.507	−0.165	−0.508
SnV(−)							
C_{2h}							
$C_{1,4}$		122.80	123.52	122.78	89.45	156.41	89.46
$C_{2,3,5,6}$		24.32	25.96	21.86	16.12	18.35	30.55
^{117}Sn	0.57	31.523	30.845	31.5	30.596	30.347	30.559
D_{3d}							
C-first neighbor		13.183	12.892	14.026	9.292	−9.237	−9.067
^{117}Sn		183.785	211.081	−22.512	−60.844	146.023	121.711
PbV(−)							
C_{2h}							
$C_{1,4}$		53.72	55.04	53.72	32.67	75.57	32.67
$C_{2,3,5,6}$		13.07	12.16	11.31	9.06	14.71	9.97
^{207}Pb		−18.15	−18.11	−18.68	−18.37	−17.57	−17.65
D_{3d}							
C-first neighbor		19.86	19.86	20.76	27.81	12.19	12.19
^{207}Pb		−793.26	−793.26	−793.26	−1004.34	−1004.34	−1004.34

- Eknamkul, D. S. Levonian, M. K. Bhaskar, H. Park, M. Lončar, and M. D. Lukin, *Nature* **629**, 573 (2024).
- [24] J. P. Goss, R. Jones, S. J. Breuer, P. R. Briddon, and S. Öberg, *Phys. Rev. Lett.* **77**, 3041 (1996).
- [25] A. Gali and J. R. Maze, *Phys. Rev. B* **88**, 235205 (2013).
- [26] G. Thiering and A. Gali, *Phys. Rev. X* **8**, 021063 (2018).
- [27] M. W. Doherty, N. B. Manson, P. Delaney, F. Jelezko, J. Wrachtrup, and L. C. Hollenberg, *Physics Reports* **528**, 1 (2013).
- [28] A. Gali, *Nanophotonics* **8**, 1907 (2019).
- [29] B. Pingault, J. N. Becker, C. H. H. Schulte, C. Arend, C. Hepp, T. Godde, A. I. Tartakovskii, M. Markham, C. Becher, and M. Atatüre, *Phys. Rev. Lett.* **113**, 263601 (2014).
- [30] J. N. Becker, J. Görlitz, C. Arend, M. Markham, and C. Becher, *Nature Communications* **7**, 13512 (2016).
- [31] P. Siyushev, M. H. Metsch, A. Ijaz, J. M. Binder, M. K. Bhaskar, D. D. Sukachev, A. Sipahigil, R. E. Evans, C. T. Nguyen, M. D. Lukin, P. R. Hemmer, Y. N. Palyanov, I. N. Kupriyanov, Y. M. Borzdov, L. J. Rogers, and F. Jelezko, *Phys. Rev. B* **96**, 081201 (2017).
- [32] J. N. Becker, B. Pingault, D. Groß, M. Gündoğan, N. Kukharchyk, M. Markham, A. Edmonds, M. Atatüre, P. Bushev, and C. Becher, *Phys. Rev. Lett.* **120**, 053603 (2018).

TABLE VII. The effective dynamic hyperfine parameters for selected ^{13}C nuclear spins in low C_{2h} symmetry for G4V(-) defects as obtained by HSE06 calculations in the electronic ground state. The directions are defined in Fig. 7(e).

Defect	A_{xx} (MHz)	A_{yy} (MHz)	A_{zz} (MHz)	A_{xy} (MHz)	A_{xz} (MHz)	A_{yz} (MHz)
Ground state						
SiV(-) - first neighbor						
A	60.4	43.2	37.5	0.0	7.2	0.0
A_x	-22.0	-6.8	-10.6	-3.0	-4.6	2.7
A_y	-50.7	-15.6	-24.4	2.3	-10.7	-2.1
SiV(-) - second neighbor						
A	-0.6	-2.7	-2.6	-0.8	0.5	-0.3
A_x	0.6	1.1	1.3	0.3	0.1	0.1
A_y	1.8	1.7	2.7	1.0	0.7	-0.6
GeV(-) - first neighbor						
A	77.6	37.0	42.0	0.0	13.9	0.0
A_x	-23.1	-11.5	-13.0	1.2	-4.0	0.4
A_y	-52.9	-26.2	-29.7	-1.0	-9.2	-0.3
GeV(-) - second neighbor						
A	-3.2	-4.3	-4.2	-1.1	-0.2	0.6
A_x	1.7	1.8	2.0	0.4	0.4	-0.4
A_y	1.5	1.9	2.7	0.3	-0.1	0.3
SnV(-) - first neighbor						
A	70.1	28.3	33.4	0.0	14.6	0.0
A_x	-21.4	-9.3	-10.8	1.3	-4.3	0.4
A_y	-49.3	-21.3	-24.9	-1.0	-9.8	-0.3
SnV(-) - second neighbor						
A	-4.1	-5.3	-4.9	-0.8	-0.2	0.5
A_x	1.9	2.1	2.1	0.3	0.4	-0.3
A_y	2.1	2.4	3.2	0.2	-0.1	0.2
PbV(-) - first neighbor						
A	60.4	39.1	33.7	0.0	9.1	0.0
A_x	-26.7	-7.4	-12.2	-4.0	-6.6	3.5
A_y	-61.6	-16.9	-28.1	3.1	-15.2	-2.7
PbV(-) - second neighbor						
A	-4.9	-5.9	-5.2	-0.6	-0.1	0.4
A_x	2.0	2.2	2.1	0.2	0.3	-0.3
A_y	2.9	3.1	3.9	0.1	-0.0	0.1
Excited state						
SiV(-)						
A	15.91	21.81	10.57	-5.13	-2.58	4.46
A_x	1.53	-4.93	0.10	2.09	0.32	-1.73
A_y	-1.10	-6.58	0.30	7.53	2.31	-3.08
GeV(-)						
A	4.80	14.61	1.43	0.94	-3.18	0.44
A_x	4.19	3.52	2.19	6.20	-1.10	-3.53
A_y	4.93	12.90	5.07	-3.26	-1.33	2.83
SnV(-)						
A	54.96	33.86	28.43	0.03	8.83	-0.02
A_x	-18.26	-3.71	-7.19	-2.77	-4.75	2.38
aA_y	-42.01	-8.31	-16.44	2.15	-10.99	-1.85
PbV(-)						
A	27.98	11.04	10.78	0.09	6.77	1.29
A_x	-7.83	0.23	-0.87	1.13	-2.18	0.12
A_y	-19.11	1.60	-2.62	-0.81	-6.72	0.75

(2018).

[33] C. Weinzetl, J. Görlitz, J. N. Becker, I. A. Walmsley,

E. Poem, J. Nunn, and C. Becher, *Phys. Rev. Lett.* **122**, 063601 (2019).

- [34] R. Debroux, C. P. Michaels, C. M. Purser, N. Wan, M. E. Trusheim, J. Arjona Martínez, R. A. Parker, A. M. Stramma, K. C. Chen, L. de Santis, E. M. Alexeev, A. C. Ferrari, D. Englund, D. A. Gangloff, and M. Atatüre, *Phys. Rev. X* **11**, 041041 (2021).
- [35] I. B. Harris, C. P. Michaels, K. C. Chen, R. A. Parker, M. Titze, J. Arjona Martínez, M. Sutula, I. R. Christen, A. M. Stramma, W. Roth, C. M. Purser, M. H. Appel, C. Li, M. E. Trusheim, N. L. Palmer, M. L. Markham, E. S. Bielejec, M. Atatüre, and D. Englund, *PRX Quantum* **4**, 040301 (2023).
- [36] W. Kohn and L. J. Sham, *Phys. Rev.* **140**, A1133 (1965).
- [37] P. Hohenberg and W. Kohn, *Phys. Rev.* **136**, B864 (1964).
- [38] P. E. Blöchl, *Phys. Rev. B* **50**, 17953 (1994).
- [39] G. Kresse and D. Joubert, *Phys. Rev. B* **59**, 1758 (1999).
- [40] G. Kresse and J. Furthmüller, *Phys. Rev. B* **54**, 11169 (1996).
- [41] G. Kresse and J. Furthmüller, *Computational Materials Science* **6**, 15 (1996).
- [42] J. Sun, A. Ruzsinszky, and J. P. Perdew, *Phys. Rev. Lett.* **115**, 036402 (2015).
- [43] J. Heyd, G. E. Scuseria, and M. Ernzerhof, *The Journal of Chemical Physics* **118**, 8207 (2003).
- [44] A. Gali, *Phys. Rev. B* **79**, 235210 (2009).
- [45] P. E. Blöchl, *Phys. Rev. B* **62**, 6158 (2000).
- [46] K. Szász, T. Hornos, M. Marsman, and A. Gali, *Phys. Rev. B* **88**, 075202 (2013).
- [47] F. S. Ham, *Phys. Rev.* **138**, A1727 (1965).
- [48] I. Bersuker, *The Jahn-Teller effect* (Cambridge University Press, Cambridge, UK, 2006).
- [49] I. Bersuker and V. Polinger, *Vibronic Interactions in Molecules and Crystals*, Springer Series in Chemical Physics (Springer Berlin Heidelberg, 2012).
- [50] S. Steiner, S. Khmelevskiy, M. Marsmann, and G. Kresse, *Phys. Rev. B* **93**, 224425 (2016).
- [51] R. Bruyndonckx, C. Daul, P. T. Manoharan, and E. Deiss, *Inorganic Chemistry* **36**, 4251 (1997).
- [52] P. Deák, B. Aradi, T. Frauenheim, E. Janzén, and A. Gali, *Phys. Rev. B* **81**, 153203 (2010).
- [53] C. Freysoldt, B. Grabowski, T. Hickel, J. Neugebauer, G. Kresse, A. Janotti, and C. G. Van de Walle, *Rev. Mod. Phys.* **86**, 253 (2014).
- [54] A. Csóré, I. G. Ivanov, N. T. Son, and A. Gali, *Phys. Rev. B* **105**, 165108 (2022).
- [55] W. Harrison, *Electronic Structure and the Properties of Solids: The Physics of the Chemical Bond*, Dover Books on Physics (Dover Publications, 2012).
- [56] G. Thiering and A. Gali, *Phys. Rev. B* **96**, 081115 (2017).
- [57] B. L. Green, S. Mottishaw, B. G. Breeze, A. M. Edmonds, U. F. S. D’Haenens-Johansson, M. W. Doherty, S. D. Williams, D. J. Twitchen, and M. E. Newton, *Phys. Rev. Lett.* **119**, 096402 (2017).
- [58] M. H. Metsch, K. Senkalla, B. Tratzmiller, J. Scheuer, M. Kern, J. Achard, A. Tallaire, M. B. Plenio, P. Siyushev, and F. Jelezko, *Phys. Rev. Lett.* **122**, 190503 (2019).
- [59] R. Monge, T. Delord, G. Thiering, A. Gali, and C. A. Meriles, *Phys. Rev. Lett.* **131**, 236901 (2023).
- [60] G. Thiering and A. Gali, “Nuclear spin relaxation in solid state defect quantum bits via electron-phonon coupling in their optical excited state,” (2024), [arXiv:2402.19418 \[quant-ph\]](https://arxiv.org/abs/2402.19418).
- [61] K. V. Kepesidis, M.-A. Lemonde, A. Norambuena, J. R. Maze, and P. Rabl, *Phys. Rev. B* **94**, 214115 (2016).
- [62] L. J. Rogers, K. D. Jahnke, M. H. Metsch, A. Sipahigil, J. M. Binder, T. Teraji, H. Sumiya, J. Isoya, M. D. Lukin, P. Hemmer, and F. Jelezko, *Phys. Rev. Lett.* **113**, 263602 (2014).
- [63] M. Haouas, F. Taulelle, and C. Martineau, *Progress in Nuclear Magnetic Resonance Spectroscopy* **94-95**, 11 (2016).
- [64] P. Pyykkö, *Molecular Physics* **106**, 1965 (2008), <https://doi.org/10.1080/00268970802018367>.